The Astrophysical Journal, 744:98 (10pp), 2012 January 10 doi:10.1088/0004-637X/744/2/98

OBSERVATIONS OF THE INTERACTION OF ACOUSTIC WAVES AND SMALL-SCALE MAGNETIC FIELDS IN A QUIET SUN

Lakshmi Pradeep Chitta[1], Rekha Jain[2], R. Kariyappa[1], and Stuart M. Jefferies[3]
[1] Indian Institute of Astrophysics, Bangalore 560 034, India; pradeepch@iiap.res.in, rkari@iiap.res.in
[2] Applied Mathematics Department, University of Sheffield, Sheffield S3 7RH, UK; R.Jain@sheffield.ac.uk
[3] Institute for Astronomy, University of Hawaii, HI 96768-8288, USA; stuartj@ifa.hawaii.edu
Received 2011 January 24; accepted 2011 September 16; published 2011 December 19

ABSTRACT

The effect of the magnetic field on photospheric intensity and velocity oscillations at the sites of small-scale magnetic fields (SMFs) in a quiet Sun near the solar disk center is studied. We use observations made by the *G*-band filter in the Solar Optical Telescope on board *Hinode* for intensity oscillations; Doppler velocity, magnetic field, and continuum intensity are derived from an Ni I photospheric absorption line at 6767.8 Å using the Michelson Doppler Imager on board the *Solar and Heliospheric Observatory*. Our analysis shows that both the high-resolution intensity observed in the *G* band and velocity oscillations are influenced by the presence of a magnetic field. While intensity oscillations are suppressed at all frequencies in strong magnetic field regions compared to weak magnetic field regions, velocity oscillations show an enhancement of power in the frequency band 5.5–7 mHz. We find that there is a drop of 20%–30% in the *p*-mode power of velocity oscillations within the SMFs when compared to the regions surrounding them. Our findings indicate that the nature of the interaction of acoustic waves with the quiet Sun SMFs is similar to that of large-scale magnetic fields in active regions. We also report the first results of the center-to-limb variation of such effects using the observations of the quiet Sun from the Helioseismic and Magnetic Imager (HMI) aboard the *Solar Dynamics Observatory* (*SDO*). The independent verification of these interactions using *SDO*/HMI suggests that the velocity power drop of 20%–30% in *p*-modes is fairly constant across the solar disk.

Key words: Sun: helioseismology – Sun: oscillations – Sun: photosphere – Sun: surface magnetism

Online-only material: color figures

1. INTRODUCTION

The magnetic field plays an important role in the evolution of the Sun. Rooted in the convection zone below the solar surface, the magnetic flux tubes extend up into the solar atmosphere and show up as sunspots, plages, networks, small bright points, etc., with very wide scales ranging from a few hundreds of an arcsecond to a subarcsecond. At the solar surface, the magnetic field offers a variety of physical phenomena by directly interacting with waves and oscillations. For example, the magnetic field interacts with the trapped acoustic waves below the acoustic cutoff (*p*-modes) and the running waves (high-ν) in different ways (suppression of *p*-modes and enhancement of high-ν waves over strong magnetic field regions). Concrete results from a wealth of literature over the past two decades show the absorption and scattering of *p*-modes by sunspots and other active regions. Also, the surface amplitudes of solar oscillations are strongly modified by the presence of the magnetic field (Leighton et al. 1962; Woods & Cram 1981; Lites et al. 1982; Braun et al. 1987, 1990; Braun & Duvall 1990; Braun et al. 1992a; Brown et al. 1992; Braun 1995; Hindman & Brown 1998; Jain & Haber 2002; Gizon et al. 2009; Schunker & Braun 2011). Thomas & Stanchfield (2000) discussed in detail the effects of fine-scale magnetic fields on *p*-modes and higher frequency acoustic waves in a solar active region. Possible mechanisms have been proposed to explain these kinds of phenomena (Jain et al. 1996, and references therein). Many interesting questions were also raised by Brown et al. (1992). For example: How is high-frequency power distributed in quiet regions where the large-scale magnetic field is weak? What is the relationship between the excess high-frequency emission and the magnetic field? How does the high-frequency excess depend on height in the solar atmosphere?

Thus, earlier works have firmly established the relation between velocity/intensity oscillations and larger magnetic structures in the active regions of the Sun. In our present work, we focus on the opposite end of the spectrum both in terms of the size of magnetic structures and the activity. We also include *G*-band intensity and Fe I 6173.3 Å velocity data, which sample different heights above the photosphere compared to the data sets used in the earlier studies of this kind. We discuss the influence of the quiet Sun magnetic field on the intensity and velocity oscillations. We consider "quiet Sun" small-scale magnetic fields (SMFs) in both surroundings, with and without any large-scale and strong magnetic activity such as sunspots or plages. This work is important in the context of the prevailing magnetic field in small scales throughout the solar disk.

In the photosphere, the SMFs are manifested as bright regions when observed using the *G*-band filter at a high resolution (Berger & Title 2001). We use the filtergram (FG) data obtained from the Solar Optical Telescope (SOT) on board *Hinode* (Kosugi et al. 2007; Tsuneta et al. 2008; Suematsu et al. 2008) for the *G*-band observations. Magnetic field strength for these bright regions seen in the *G* band is derived from the quasi-co-temporal observations obtained from the Michelson Doppler Imager (MDI; Scherrer et al. 1995) on board the *Solar and Heliospheric Observatory* (*SOHO*) and *Hinode* SOT/spectropolarimeter (SP). For a detailed analysis of the nature of the velocity field at the sites of SMFs, we combine observations from the *SOHO*/MDI and Helioseismic and Magnetic Imager (HMI) on the *Solar Dynamics Observatory* (*SDO*).

Table 1
Details of the Data Sets Used

Instrument	Date and Time of Observation	Duration (hr)	Cadence (minutes)	Pixel Area
Hinode SOT/FG				
G band	2007-04-13T19:00–21:00 (set 1)	2	0.5	0.″108 × 0.″108
	2007-06-24T17:08–18:13 (set 2)	∼1	1	0.″108 × 0.″108
Magnetograms, Dopplerograms, and High-Resolution FG				
Hinode SOT/SP	2007-06-24T17:08–18:13	∼1	...	∼0.″3 × 0.″32
	2001-12-21T00:00–05:00	5		
	2004-05-23T15:00–20:00	5		
SOHO/MDI	2007-04-13T19:00–21:00 (set 1)	2	1	0.″6 × 0.″6
	2007-06-24T17:00–19:11 (set 2)	2.2		
	2009-04-18T15:00–20:00	5		
	2010-09-12T00:00–03:00 (type (a))			
SDO/HMI	2010-10-17T00:00–03:00 (type (a))	3	0.75	0.″5 × 0.″5
	2010-10-30T00:00–03:00 (type (a))			
	2010-10-20 – 21T17:19–22:07 (type (b))	28.8	0.75	0.°04 × 0.°04

Such a unique combination of observations from different instruments is desired to exclude any spurious outcome. In this paper, we study the interaction of SMFs with velocity/intensity oscillations at different frequencies and how the intensity and acoustic power varies as a function of magnetic field strength across the solar disk for particular frequency ranges.

The findings and results reported in this paper are based on the analysis carried out on a number of data sets taken from different days. The paper is organized as follows. Section 2 deals with the details of various observations used for the analysis. In Section 3, we examine the relation between the magnetic-field–velocity oscillations and magnetic-field–intensity oscillations. In Section 4, we discuss these results with concluding remarks.

2. DATA SETS

We consider different data sets of *G*-band FGs, magnetograms, Dopplerograms, and high-resolution FGs for this analysis. Table 1 gives a summary of the data sets used for the analysis. The details of these data sets are as follows.

2.1. Disk Center

G-band data from Hinode SOT/FG: Set 1—Time series with a resolution of 0.″108 pixel^{-1} and a 111″ × 55″ field of view (FOV), with a 30 s time cadence obtained near the disk center (17.″30, −24.″35), on 2007 April 13 at 19:00– 21:00 UT. Set 2—Time series with a resolution of 0.″108 pixel^{-1} and a 111″ × 111″ FOV, with a 1 minute time cadence obtained near the disk center (−9.″88, 32.″53) in a quiet region on 2007 June 24 at 17:08–18:13 UT. From these *G*-band data cubes, we extract and use only the regions for which magnetic field information is available. *Magnetograms, Dopplerograms, and high-resolution FGs*: high-resolution observations from *SOHO*/MDI with a resolution of 0.″6 pixel^{-1} and about a 600″ × 300″ FOV with a 1 minute time cadence, obtained quasi-simultaneously with Set 1 of the *G*-band data. Also, data sets obtained on 2001 December 21, 2004 May 23, 2007 June 24, and 2009 April 18 and co-temporal level-1d *Hinode* SOT/SP data corresponding to Set 2 of the *G*-band data are considered for the analysis.

Hinode/SOT's FOV is completely contained within the *SOHO*/MDI's FOV. *G*-band FGs are processed to level-1 data using standard procedures provided in the *solarsoft* library

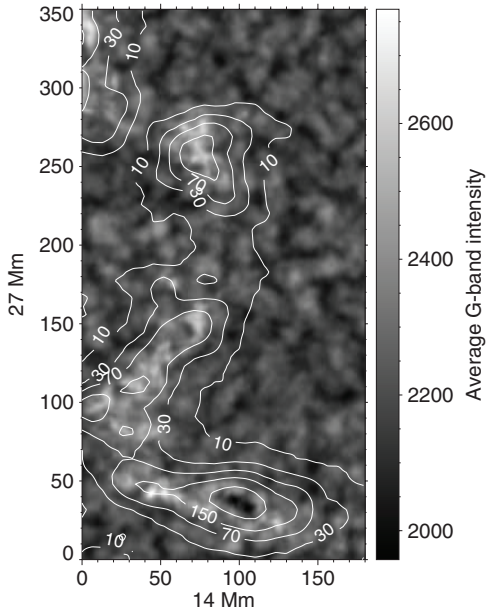

Figure 1. Contours for various values of mean magnetic field strength (in Gauss) obtained from *SOHO*/MDI are overplotted on the time averaged *G*-band (Set 1) intensity map. Note that this map corresponds to the central region (marked within the black rectangle) of Figure 2.

(Freeland & Handy 1998). MDI data are processed to level 1.8. *Hinode* SOT/SP inversions were conducted at NCAR under the framework of the Community Spectro-Polarimetric Analysis Center (http://www.csac.hao.ucar.edu/). We invariably mention the longitudinal apparent magnetic flux density (derived from *SOHO*/MDI, *Hinode* SOT/SP, and *SDO*/HMI) as the magnetic field strength in the rest of this paper.

For this analysis, we have identified a network region from Set 1 and small networks and bright points from Set 2 of the *G*-band time series. The selected regions show enhanced brightness compared to the surrounding granules. We plot the map of the region of interest from Set 1 (see Figure 1). The selected bright feature has a counterpart in the magnetograms, for which the magnetic field strength has a range of values from −457 to 228 G in a 2 hr time-averaged magnetic map obtained from the time series. We also have corresponding Doppler images (Figure 2) and high-resolution FGs from MDI.

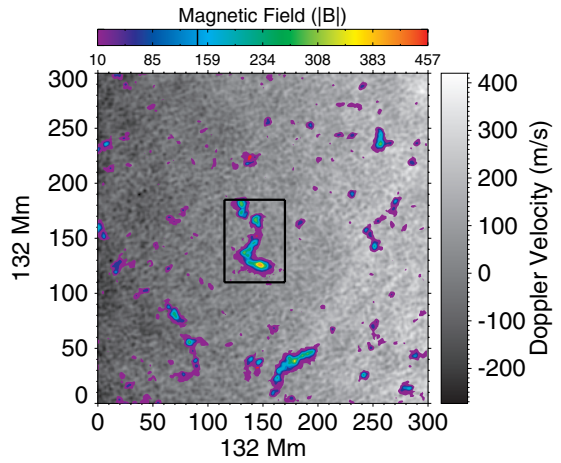

Figure 2. Shown in the gray scale is a sample of the 2 hr time-averaged Doppler image obtained from *SOHO*/MDI on 2007 April 13. Colored contours indicate the location of the mean magnetic field (absolute value) obtained from MDI magnetograms. Note that the central region marked in the black rectangle is the location of *G*-band (Set 1) observations (see Figure 1).

(A color version of this figure is available in the online journal.)

High-resolution *G*-band images are resized and aligned to match MDI high-resolution FGs. A portion corresponding to the *G*-band FOV is extracted from the velocity, intensity, and magnetic field data sets for the analysis. An average magnetic field map is formed using the extracted magnetograms. The contours of magnetic field strength are shown in Figure 1. Note, for the analysis of magnetic field dependence on the velocity oscillatory power, we use a much larger FOV (a sample region is shown in Figure 2), keeping the image resolution to $0\farcs6$ pixel^{-1}, i.e., the original image resolution of MDI. The above-mentioned intensity (both *G*-band and high-resolution FGs) and Doppler velocity data sets are Fourier transformed in time at each pixel to obtain the power spectra of intensity and velocity fluctuations for each pixel.

2.2. Center to Limb

Since we are dealing with small-scale features on the Sun, to carry out the longitudinal variation of the magnetic-field–Doppler-velocity relation, we need simultaneous and precise observations of velocity oscillations and magnetic field across the solar disk. *SDO*/HMI is capable of providing high-quality rapid and simultaneous full-disk observations with virtually no data gaps. *SDO*/HMI uses the Fe I 6173.3 Å line for both Doppler velocity and line-of-sight (LOS) magnetic field measurements. To avoid any ambiguity, we consider five data sets for which observations are made on September 12 and October 17, 20, 21, and 30 of 2010 using *SDO*/HMI. In the above-mentioned observations, there are two data types: (a) Doppler velocity and magnetograms of September 12, October 17, and October 30 and (b) Doppler velocity and magnetograms of October 20 and 21 that are tracked and re-mapped into heliographic coordinates (using Postel's projection) corresponding to Carrington rotation 2102. The image resolution is set to $0\farcs504$ pixel^{-1} and $0\fdg04$ pixel^{-1} for data types (a) and (b), respectively.

Data type (a) is a set of Doppler velocity and LOS magnetic field observations of a 3 hr duration for each day. Using *hg_patch* mode (at http://jsoc.stanford.edu/ajax/exportdata.html), we select cuts of $1800'' \times 300'' \times 3$ hr data cubes (read as width × height × time). Since our desire is to study the strength of the interaction from the center to the limb, we make smaller data cubes of $200'' \times 300'' \times 3$ hr from the above-mentioned sets. For representation, in Figure 3, we show a map of Doppler velocity from the time series of 2010 October 17. The black rectangles represent three regions of analysis centered at $(-400'', 0'')$, $(0'', 0'')$, and $(400'', 0'')$, respectively, and the overlapping dashed white rectangles are also regions of analysis centered at $(-300'', 0'')$ and $(300'', 0'')$. In total, we extract 17 smaller cubes from each full data cube, and the smaller cubes have an overlap of $100''$ in the *x*-direction of the image plane as shown in Figure 3 with their adjacent regions. Data type (b) is composed of Doppler velocity cubes of $15^\circ \times 15^\circ \times 28.8$ hr observed at five positions on the solar disk, i.e., corresponding to five solar longitudes. For better comparison, we extract two 3 hr duration subsets from each data cube (along with the magnetograms), the *first* set at the beginning and the *second* close to the middle of the observations with a 12 hr time gap between two extracted subsets. Hereafter, we call the *first* subset b_1 and the *second* subset b_2. We feel that the time gap we consider is long enough compared to the timescales of rapidly evolving SMFs, which ensures a different morphology and configuration of the magnetic field in the former and latter subsets at any particular longitude.

All the velocity cubes (data types (a) and (b)) are Fourier transformed in time at each spatial point and the acoustic power is determined with a frequency resolution of 93 μHz up to the Nyquist frequency of 11.11 mHz. The resultant cubes are then integrated over the frequency ranges 2.5–3.9 mHz and 5.5–7 mHz to construct *p*-mode and high-ν power maps, respectively.

3. RESULTS

3.1. Influence of the Magnetic Field on Velocity Oscillations

Power maps of trapped *p*-mode and high-ν oscillations are obtained from the power spectra by integrating the power over all

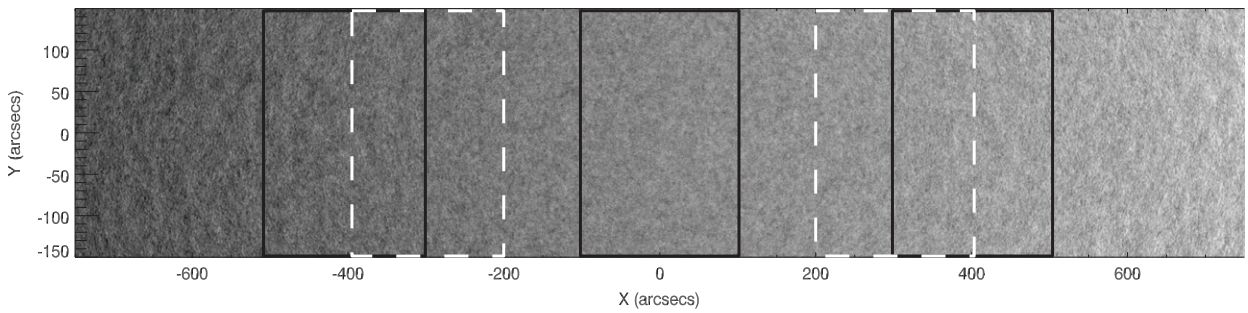

Figure 3. Sample image of Doppler velocity taken from data of 2010 October 17 (type (a)). The image is centered at $(0'', 0'')$. For representation, three black rectangles of $200'' \times 300''$ are shown corresponding to three extracted regions used for the analysis, centered at $(-400'', 0'')$, $(0'', 0'')$, and $(400'', 0'')$, respectively. To demonstrate the overlapping, dashed white rectangles are drawn centered at $(-300'', 0'')$ and $(300'', 0'')$ which are also used for the analysis.

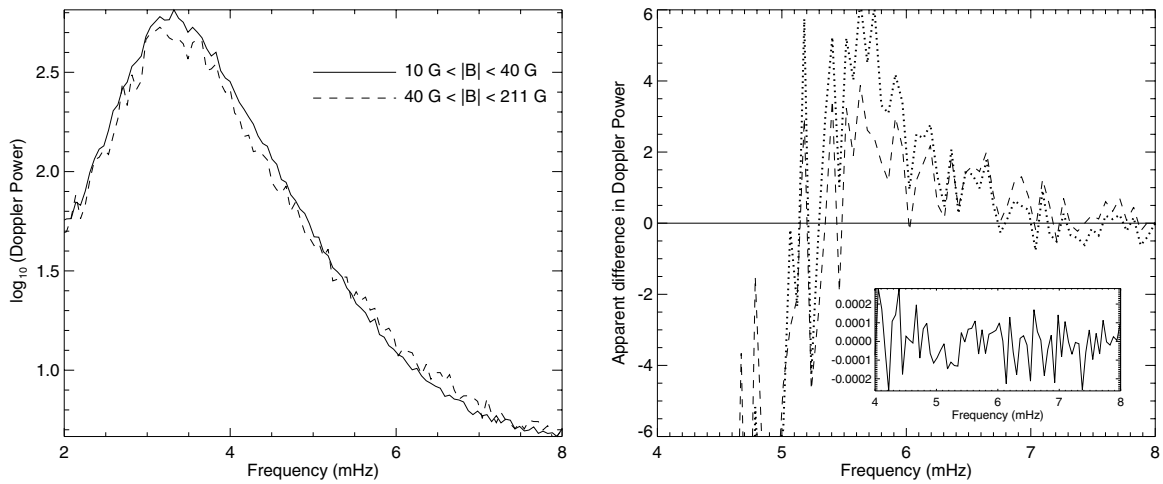

Figure 4. Left panel: $\log_{10}$ of the observed Doppler VP observed (for the 2009 April 18 data) for two ranges of magnetic field strengths $10 < |B| < 40$ G (solid line) and $40 < |B| < 211$ G (dashed line). Note that the enhancement is seen in high-ν waves (above 5.5 mHz) in the strong field case whereas the p-modes are suppressed. Right panel: apparent difference in the Doppler VP observed for the original data (dashed line) and modeled noise data (solid line). The inset shows the variations in the solid line (i.e., NP) in the 4–8 mHz band. The dotted line shows the Doppler power increment over strongly magnetized regions in comparison with power over very weakly magnetized (0–5 G) regions (see the text for details).

frequencies at each pixel within the ν-range $2.5 \leqslant \nu \leqslant 3.9$ mHz and $5.5 \leqslant \nu \leqslant 7$ mHz, respectively. We plot the velocity power (VP) as a function of magnetic field strength. A gradual decrease in the VP in the frequency band $2.5 \leqslant \nu \leqslant 3.9$ mHz is observed with increasing field strength. In the left panel of Figure 4, we plot the VP as a function of frequency. An enhancement in the VP is clearly seen for frequencies above 5.5 mHz (dashed line) compared to their profile over weak magnetized regions (solid line), differing from the nature of p-mode behavior. Furthermore, to determine the strength of the interaction of velocity oscillations and magnetic field in the quiet Sun regime, we calculate a ratio from the average p-mode powers in the regions corresponding to $10 < |B| < 40$ G and $|B| > 40$ G. We chose these field strength ranges because we identified that the regions with $10 < |B| < 40$ G form a boundary surrounding the SMFs whereas the regions with $|B| > 40$ G form the interior regions of these magnetic elements. We find that there is a drop of ∼20%–30% in the p-mode power in the interior regions. This drop in power is consistent from our analysis of many data sets. To compare this ratio with the values over active regions, we calculate the ratio in the case of large magnetic structures, such as plages and sunspots, for other data sets (not shown here) and find that there is more than a 30%–40% drop in the p-mode power in such large active regions for high magnetic field strengths.

It is worthwhile to analyze the contribution of random noise (for example, ± 20 m s^{-1} noise per pixel in the *SOHO*/MDI Doppler velocity data) to the power spectrum as a function of frequency. For this, we have generated a random noise data cube of the same dimensions (both in space and time) as that of analyzed Doppler velocity data. A red noise power (NP) spectrum (power decreases with the increase in frequency) has been obtained from the Fourier transformation of noise data in the time domain. The NP integrated over weak and strong magnetic field strengths has been compared with the MDI VP. It is also essential to compare the enhancement seen in high-ν over strong magnetized regions with the power over very weakly magnetized (over 0–5 G) regions ($P_{0-5\,\mathrm{G}}$). The results are shown in the right panel of Figure 4, for which the description of contents is as follows. Solid line: derived from noise data → $\mathrm{NP_{strong}} - \mathrm{NP_{weak}}$ (also shown in the inset); dashed line: derived from the MDI signal → $\mathrm{VP_{strong}} - \mathrm{VP_{weak}}$; dotted line: derived from the MDI signal → $\mathrm{VP_{strong}} - P_{0-5\,\mathrm{G}}$; strong and weak in the above description denote the magnetic field strengths. $\mathrm{NP_{strong}} - \mathrm{NP_{weak}}$ is read as $\mathrm{NP_{strong}}$ minus $\mathrm{NP_{weak}}$. These results suggest that a noise of ± 20 m s^{-1} may contribute a negligible amount of power to the original signal. We implemented this comparison using white noise (power is constant as a function of frequency), and we do not see any substantial changes in the result. This confirms that the noise in the pixel counts will not possess a well-defined power profile with respect to the magnetic field. The power increment seen above 5.5 mHz in the strong field regions as compared to that of very weakly magnetized (0–5 G) regions (dotted line) is consistent with the earlier works on active regions (for example, Figure 5 in Brown et al. 1992).

3.1.1. True Quiet Sun

Even the "quiet" regions far away from magnetically active regions consist of SMFs with shorter timescales. The solar surface is filled with such a ubiquitous, turbulent magnetic field with short lifetimes, which may govern the dynamics of the solar atmosphere. Such a turbulent magnetic field is generated and sustained by a local dynamo phenomenon that is believed to occur at granular scales. For a recent review on different possible generation mechanisms of SMFs, see de Wijn et al. (2009). By investigating the influence of these small-scale fields on observed Doppler velocities, we can in turn start unraveling the influence of the source(s) of these kinds of magnetic fields on the oscillatory behavior at the solar surface. It is therefore interesting to quantify the contribution toward suppression/enhancement of oscillatory power from such quiet Sun regions alone.

One direct way to do this is by quantitatively comparing the results from the regions with different surroundings. This will enable us to see the possible influence (if any) of the surroundings on the region of interest. Thus, we analyze three different regions: (1) a relatively quiet Sun near a big sunspot, (2) a region far from a sunspot group, and (3) a true quiet Sun. We carefully choose the true quiet Sun regions such that there are no large-scale activities in the observable part of the solar disk up to at least 10 days before observation. For better and easier comparison, it is useful to keep the spatial dimensions and time span of observations fixed in all three cases. For

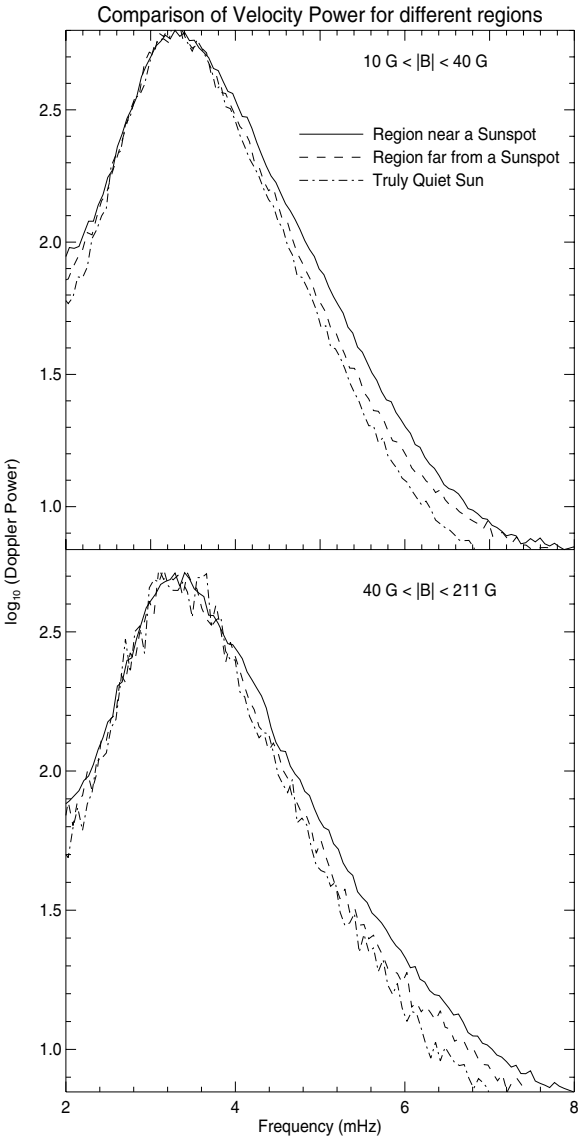

Figure 5. Comparison between the Doppler VPs for three different regions with different surroundings. Top panel: VP for magnetic field strengths $10 < |B| < 40$ G in a relatively quiet region close to a sunspot (solid line), far from a sunspot group (dashed line), and in a truly quiet Sun (dash-dot line). Bottom panel: same as the top panel, but for field strength ranging in $40 < |B| < 211$ G. Difference in the three regions is seen in both weak and strong field cases above 4 mHz.

this, we choose a region of $240'' \times 240'' \times 5$ hr from each data set (2001 December, 2004 May, and 2009 April). These three periods correspond to different phases of solar activity. To compare the oscillatory behavior over similar field strengths, we set the field strength ranges with respect to the quiet Sun magnetic field as discussed earlier. We plot the Doppler VP as a function of frequency for all three cases (Figure 5). Top and bottom panels are for weak ($10 < |B| < 40$ G) and strong ($40 < |B| < 211$ G) field ranges, respectively. In both panels, solid, dashed, and dash-dot lines represent 2001, 2004, and 2009 data, respectively. We see that for the same field strength ranges (in both weak and strong field cases), the distinction becomes evident between the three regions above 4 mHz. The VP signal is generally found to be more suppressed in the "true quiet region" compared to the quiet regions nearer or farther away from the sunspots, for both magnetic field ranges. However, the power ratio (strong to weak magnetic field strengths) within the FOV as a function of frequency is found to be the same for all three data sets, suggesting that the relative difference in the Doppler VP between non-magnetized and magnetized regions is independent of the proximity of the small-scale magnetic features to the large magnetic active regions. This similarity in the qualitative behavior of all three data sets would suggest that the same physical mechanism (for power suppression (enhancement) below (above) 5.5 mHz) is at play regardless of whether the quiet region is closer to an active region or not. However, one of the concerns is that a change in the modulation transfer function of the MDI instrument over time could also lead to a slight change in the magnitude of the observed Doppler velocities in the surroundings, so some caution is necessary when interpreting these results.

3.2. Center-to-Limb Variation (CLV) of the Interaction

The nature of the *p*-mode power enhancement (sometimes referred to as the "acoustic halos") above 5 mHz is not very clear to date. Braun et al. (1992b) and Brown et al. (1992) interpret this phenomenon describing high-ν halos as the regions with increased acoustic emissivity or scattering. Hindman & Brown (1998) suggested that the magnetic field, which is primarily vertical at the photosphere, ducts the acoustic oscillations into field-aligned motions and, therefore, observations at the disk center would register an increased LOS velocity signal.

One would ideally expect to examine the same magnetic feature and its interaction with its surroundings at different positions as it traverses across the solar disk, but since we are limited by the rapid evolution of small-scale magnetic features and these features reconfigure very fast (having a smaller lifetime compared to the solar rotation), the results may not be actually driven by the configuration of the field alone but may depend on the position. We try to qualitatively show that this assumption is indeed not far from the true behavior of these features. To this end, we sort the *p*-mode and high-ν VP maps with the magnetic field. Now, we consider two ranges of magnetic fields: $10 < |B| < 40$ G (weak field) and $|B| > 40$ G (strong field), then take the average powers within the respective magnetized regions and take the ratio of the average VP in the strong field to the weak field (for both frequency bands). In Figure 6, we show the ratios calculated in the manner described above and plot for various positions across the solar disk. The left panel of Figure 6 shows the results obtained from data type (a),[4] where the *open symbols* denote the *p*-mode ratio and *solid symbols* are for the high-ν power, and the *x*-axis is the distance measured in arcseconds on either side of the disk center. While the ratio of *p*-mode power is constant around a value of 0.8 (this value is consistent with the disk center results obtained from *SOHO*/MDI) across the solar disk, the high-ν power ratio decreases from center to limb. The right panel of Figure 6 is the same as the left panel but plotted for the power maps of data type (b); the *x*-axis denotes the central meridian (Stonyhurst units) of the tracked region at the mid-time of tracking. Power ratios corresponding to $+70^{\circ}$ have some deviation from the regular trend; this is largely due to the fact that the limbward data are affected in the course of tracking and remapping (this can be noticed in the movies of limbward velocity data).

We must admit that selecting the field ranges arbitrarily could be misleading and hence a further scrutiny is required. A careful

[4] Plot is for the mean value of ratios derived from the three sets and the error bars showing 1σ deviation from the mean.

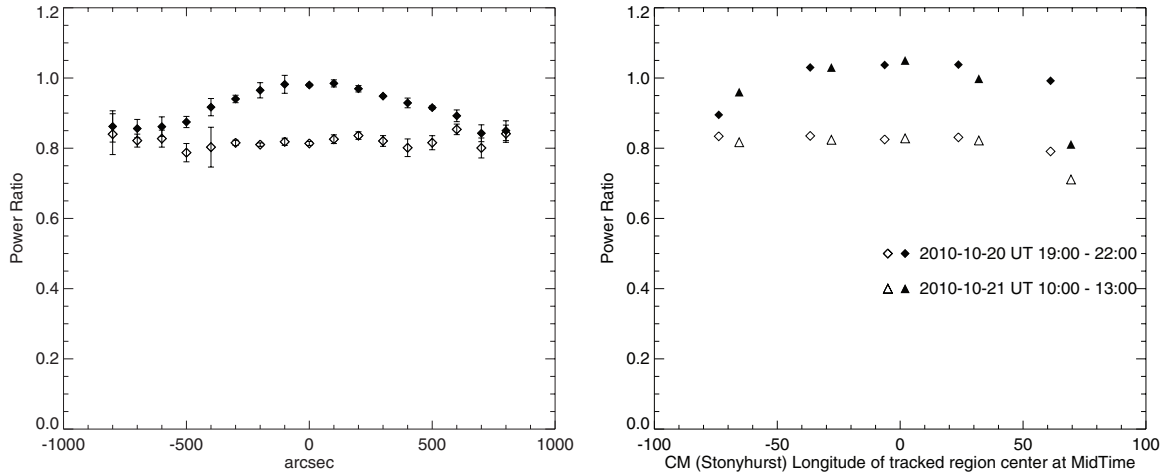

Figure 6. $P_{\rm I}$ is the average VP over regions with a weak magnetic field ($10 < |B| < 40$ G) and $P_{\rm II}$ is the average VP over regions with a strong magnetic field ($|B| > 40$ G). We plot the ratio $P_{\rm II}/P_{\rm I}$ for both p-modes (open symbols) and high-ν (solid symbols) oscillations across the solar disk for data type (a) (left panel, tracked data sets) and data type (b) (right panel, data sets tracked and remapped using Postel projections).

analysis of the VP and the connection with the magnetic field gives us more insight into the connection between the two quantities, which is not obvious from Figure 6. We calculate the average power of the regions over the magnetic field ranges: 0–10, 10–20, 20–40, 40–60, >60 G in both power maps at each longitude position of data type (b) and normalize it with the maximum average power at that position:

$$r = \frac{\langle p(\nu, L_p, b_i)\rangle}{\max(\langle p(\nu, L_p, b_i)\rangle)}; \quad i = 1, 2,$$

where $\langle p(\nu, L_p, b_i)\rangle$ represents the average power at a given L_p (central meridian of the tracked region at the mid-time of tracking) in the frequency band ν (p-mode or high-ν) and r is the normalized power ratio. Here, $i = 1$ corresponds to the data cubes taken from the beginning of data type (b), while $i = 2$ is for data sets taken from the mid-time of tracking data type (b).

In this manner, we can relatively compare the behavior of p-mode and high-ν power at various positions as a function of the magnetic field. We plot this normalized power with respect to various increasing field strength ranges in Figure 7. Solid and dashed lines are for p-mode and high-ν mean normalized powers, respectively, for all longitudes. Interestingly, on a relative scale, the way p-modes interact with the magnetic field seems to be the same over a wide range of longitudes. There is a clear drop in the power when we go from weak to strong magnetic field regions. On the other hand, high-ν waves have a different route to follow. The normalized power gradually increases with an increase in the magnetic field, peaks in the range of 40–60 G, and decreases in regions of stronger field strength. This is consistent with the earlier findings reported by Jain & Haber (2002).

3.3. Influence of the Magnetic Field on Intensity Oscillations

Like velocity oscillations, intensity oscillations exhibit a coupling with the magnetic field. Similar to the VP maps, we integrate the power spectra of G-band time series in frequency ranges of $2.5 \leqslant \nu \leqslant 3.9$ mHz and $5.5 \leqslant \nu \leqslant 7$ mHz for respective intensity power maps. Figure 8 shows integrated and averaged G-band intensity power for the above-mentioned ν-bands as a function of the magnetic field. The solid line marked in the two panels shows the trend of intensity power at various

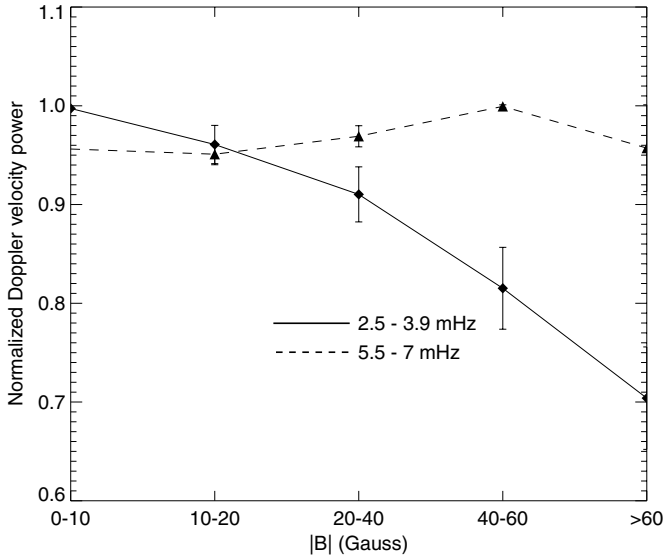

Figure 7. Mean of normalized Doppler VP (see the text) as a function of magnetic field ranges shown in the x-axis for various data sets from data type (b). Note the difference in behaviors of the acoustic p-mode (solid line) and high-ν powers (dashed line) with respect to the magnetic field.

field strengths (vertical error bars show 1σ standard deviation from the trend). Although there is an intrinsic suppression of G-band power at higher frequencies, for a given frequency band there is a further suppression observed over the strong magnetic regions. To see the power accumulation in the region of interest, we extract the G-band (Set 1) intensity power map at 3.3 mHz (where the velocity signal peaks) using a Gaussian filter with 0.5 mHz FWHM. In Figure 9, we show the contours (in blue) of regions with power $\geqslant$30% of maximum power on a time averaged intensity map. The suppression of intensity power is observed at the sites of magnetic fields seen as a bright patch in the G band (also see Figure 1).

Unlike VP, intensity oscillations (both G-band and high-resolution continuum intensity) do not show power enhancement in the ν-band 5.5–7 mHz. The power decreases for all frequencies with an increase in the magnetic field strength (see the left panel of Figure 10). We plot $\log_{10}$ of the intensity

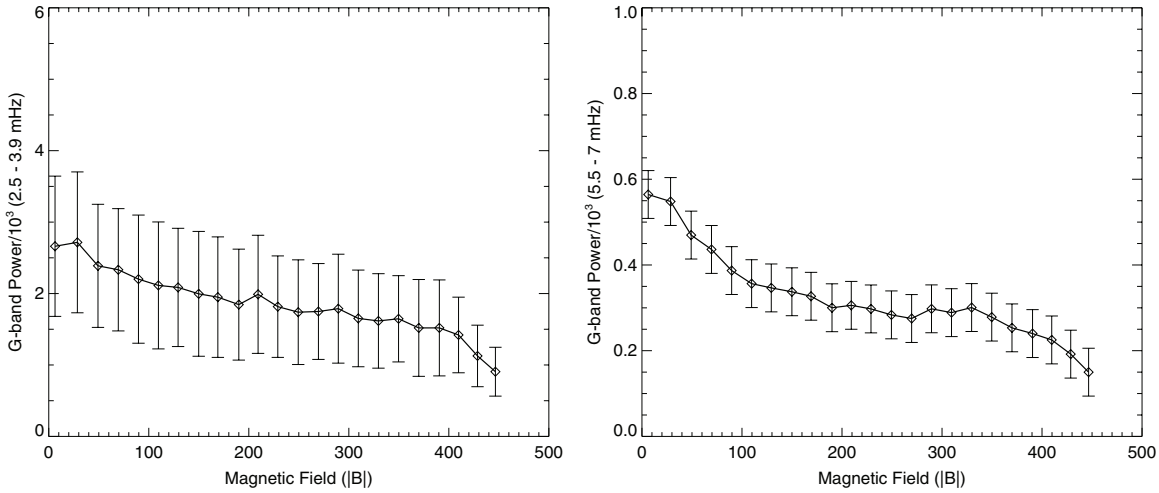

Figure 8. *G*-band (Set 1) intensity power, integrated over the frequency ranges (left) $2.5 \leqslant \nu \leqslant 3.9$ mHz and (right) $5.5 \leqslant \nu \leqslant 7$ mHz at each pixel for the region shown in Figure 1 as a function of magnetic field strength. Mean power for respective ν-bands is plotted as a function of mean field strength.

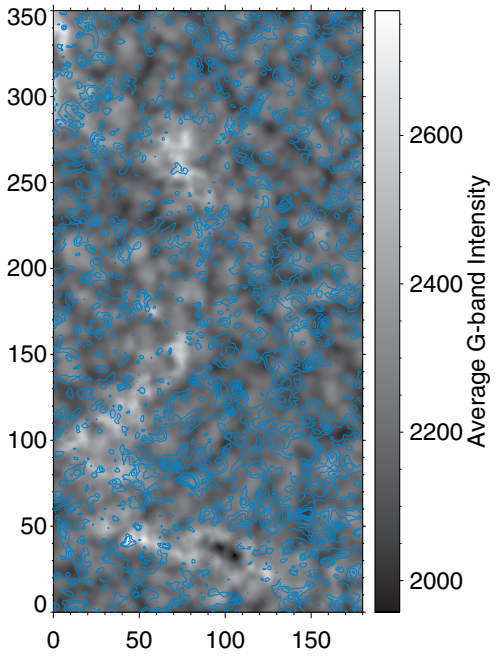

Figure 9. 3.3 mHz component of *G*-band intensity power (in blue contour) is plotted over a 2 hr average *G*-band (Set 1) intensity map. The contours are drawn for the regions between 0.3–1.0× maximum *G*-band power at 3.3 mHz. Note that the *G*-band intensity power is suppressed in the regions of magnetic fields (also see Figure 1).

(A color version of this figure is available in the online journal.)

power as a function of frequency for magnetic field[5] ranges (1) $10 < |B| < 100$ G (solid line), (2) $100 < |B| < 200$ G (* * * * line), and (3) $200 < |B| < 457$ G (dashed line). It is clear from the plot that for a given frequency, suppression increases with an increase in the magnetic field strength. The right panel of Figure 10 is a plot of $\log_{10}$ of fractional *G*-band intensity power, which is the ratio of intensity power at each frequency over the total intensity power plotted as a function of frequency for magnetic field ranges (1) $10 < |B| < 40$ G (solid line) and (2) $40 < |B| < 457$ G (dashed line).

The left panel of Figure 11 is the same as the right panel of Figure 10, except that the plot is for magnetic field[6] ranges (1) $10 < |B| < 40$ G (solid line) and (2) $40 < |B| < 521$ G (dashed line) of the 2007 June 24 data. The main difference in the two data sets is the configuration of the magnetic field. While Set 1 data cover a network region, Set 2 data are more of a scattered field of smaller units in size.

It is clear that both the intensity and velocity oscillations show power suppression with the increase in the magnetic field strength in the *p* band. It is interesting to see how this oscillatory power (say at 3.3 mHz, where VP is maximum) varies as a function of magnetic field strength. To examine this, the power spectra are filtered using a Gaussian filter of 0.5 mHz FWHM peaking at 3.3 mHz. From the resulting power maps, we calculate the average power for velocity and intensity fluctuations as a function of field strength. The spatial pixels of power maps are sorted with respect to the magnetic field. We then use a 30 G bin to segment the power maps. The average values of power and magnetic field are obtained from each segment. In the right panel of Figure 11, we plot the average powers of both velocity (◇) and *G*-band, Set 1 (△) for 3.3 mHz as a function of mean magnetic field strength with a bin size of 30 G. The slopes of least-squares fit for velocity (solid line) and *G*-band (*dashed line*) powers indicate a similar nature of reduction in velocity and intensity oscillatory powers with increase in the magnetic field strength.

The important result from these observations is that the "acoustic halos," which are ring-like regions of enhanced acoustic power in the high-ν band surrounding the magnetically active regions as described by Braun et al. (1992a) and Brown et al. (1992) are also seen surrounding very small localized fields. These "halos" can be seen as an enhancement in VP in the $5.5 < \nu < 7$ mHz band in Figure 4. The power spectrum of intensity fluctuations does not show the presence of such power enhancements or "halos" (see Figure 10).

4. DISCUSSION AND CONCLUSIONS

We used *G*-band intensity data to search for correlations between the small-scale *G*-band bright points and the corresponding underlying photospheric magnetic field and Doppler velocities. The main conclusion we draw is that the *G* band, continuum

[5] Magnetic field values are obtained from *SOHO*/MDI observations.

[6] Magnetic field values are obtained from *Hinode* SOT/SP observations.

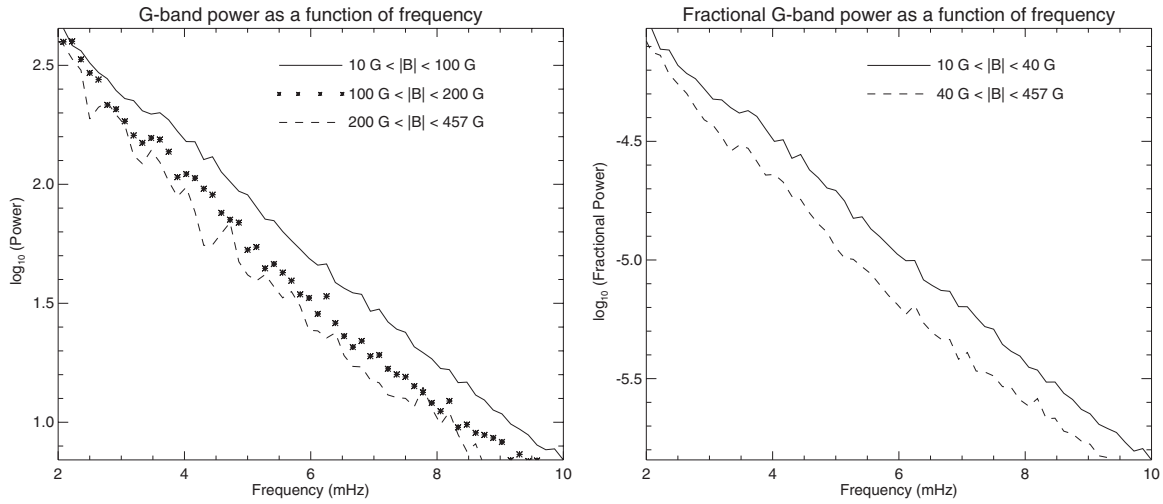

Figure 10. *G*-band (Set 1) power and fractional *G*-band power as a function of frequency for different ranges of magnetic field strengths for the region shown in Figure 1. Note that both power and fractional power of *G*-band intensity oscillations show suppression above 2 mHz with an increase in the magnetic field.

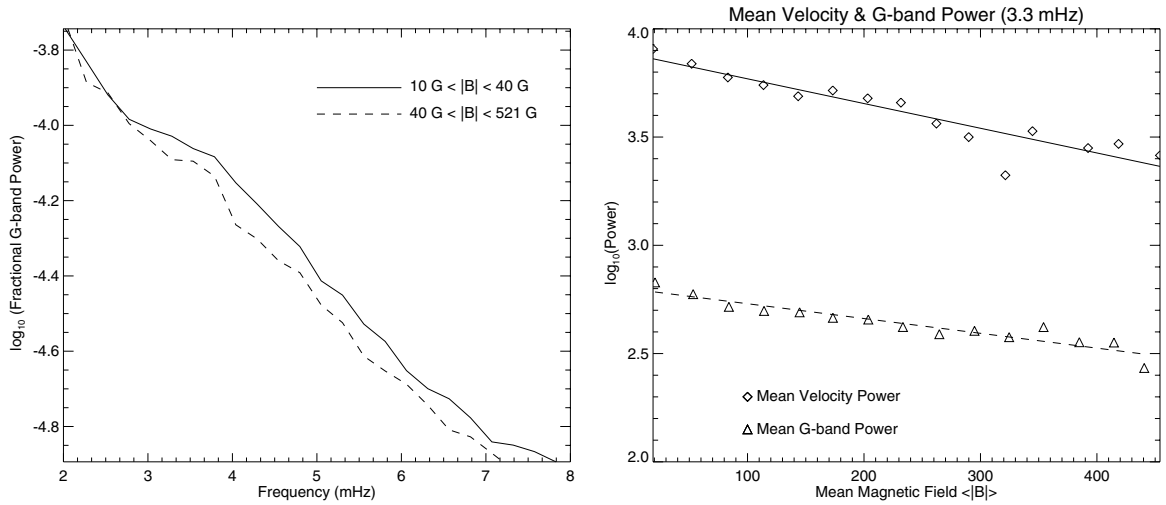

Figure 11. Left panel: same as the right panel of Figure 10 plotted for Set 2 of *G*-band data. Suppression is seen in intensity oscillations above 2 mHz. Right panel: $\log_{10}$ of mean VP (◇) and mean *G*-band (Set 1) intensity power (△) at 3.3 mHz for the regions shown in Figures 1 and 2, respectively, as a function of mean magnetic field strength obtained from binning the time averaged magnetic field strength with a 30 G bin. Solid and dashed lines show the least-squares fit for respective powers.

intensity, and Doppler VP are all influenced by magnetic fields and show power suppression in the *p* band ($\nu < 5$ mHz). The *G*-band and continuum intensity power also show suppression at high frequencies ($\nu > 5.5$ mHz) whereas the Doppler VP shows enhancements. Also, the small-scale magnetic features show this behavior everywhere, irrespective of their surroundings (i.e., nearer or farther away from a large-scale magnetic region).

What causes the power suppression in *G*-band bright points? The current analysis on MDI and *G*-band intensity data sets suggests that the suppression seen in high frequency is independent of the height, at least for the spatial resolution used in this study. This implies that the physical mechanism responsible for the power suppression in intensity data does not occur in the upper atmosphere. Also, the small-scale bright points in the *G* band and their association with the magnetic field at the photospheric height may mean that this physical mechanism is linked to magnetism. There could be changes in the radiative transfer properties or changes in wave excitation due to magnetic fields, which could lead to such variations in the power spectra. It has been reported by Bogdan et al. (1996) that the buffeting of solar acoustic waves (*p*-modes) by thin magnetic flux tubes excites magnetohydrodynamic (MHD) tube waves such as *sausage* and *kink* tube waves (see also Spruit 1984). These tube waves propagate up and down the flux tubes carrying energy away from the *p*-modes, causing damping and absorption in *p*-mode power (see Hindman & Jain 2008; Jain et al. 2009). Jain et al. (2009) theoretically calculated the energy loss in the acoustic waves due to their interaction with thin magnetic flux tubes and compared their acoustic wave absorption results with helioseismic measurements of plages. However, the thin magnetic flux tubes are present everywhere on the Sun and, although the current observational resolution limits our capability to see deeper into slender flux tubes in detail, in this study we have shown that small-scale magnetic features that may be comprised of many slender flux tubes show acoustic power suppression inside the magnetic features compared to their surroundings. The power suppression must be linked to the excitation of MHD waves.

As for the power enhancement above 5 mHz, there have been some recent investigations. A numerical investigation by Kitiashvili et al. (2011) for low angular degree modes shows interesting results. They suggest that the power suppression for

resonant modes is more for vertical magnetic fields compared to inclined fields. They also found that the power is shifted toward higher frequencies when magnetic fields are inclined. This could qualitatively explain the existence of power enhancement seen around magnetic features, but further detailed quantitative investigations are necessary before this argument can be accepted.

Why the Doppler VP shows enhancement at high frequencies is also addressed by Khomenko & Collados (2009) on the basis of a sunspot simulation. They suggest that the acoustic halos are a result of the refraction of high-frequency fast waves from the regions above the equipartition layer. Since the frequencies of trapped *p*-modes below the cut-off frequency do not reach the equipartition layer, these trapped modes do not contribute to the refraction process. Also, the halos are not seen in the umbral parts of the sunspot because the spectral line (and hence the height of observation) is above the height where refraction occurs (see also Jain & Haber 2002, regarding the argument on the spectral line formation in magnetic and non-magnetic regions). Thus, in their simulations, significant halos are seen where the magnetic field is inclined by about 30°–40°. The power enhancement ratio analyzed in this paper shows a slight decrease from center to limb and in the absence of any information on the geometry of the field lines, it is not clear whether the small-scale magnetic features have such a large angle of inclination at photospheric heights. Also, any theory that explains the Doppler power enhancement requires addressing the simultaneous suppression seen in the intensity data at and above the photospheric heights.

The absence of power enhancement in intensity data leads one to believe that the enhancement may be due to the excitation of incompressible kink tube waves at the edges of magnetic tubes (see, for example, Hindman & Brown 1998). A quantitative analysis for this mechanism is still awaited.

Another relevant point is that small-scale magnetic features such as the ones studied in this paper may also act as a local inhomogeneity, which scatters acoustic waves that are incident on them at various angles. Gordovskyy et al. (2009) and Hanasoge (2009) had suggested on the basis of the simulation of trapped *p*-modes that power is channeled from high mode-mass to low mode-mass *p*-modes resulting in a power increase for the high wavenumber part of the *p*-mode spectrum. Thus they suggested *mode mixing* as the mechanism for power enhancement seen in high frequencies. Further investigations into this issue are required as the power enhancement is generally seen for frequencies way beyond the cut-off frequencies of *p*-modes. Also, the amount of scattering will depend on the inclination of field lines, and hence on the height in the solar atmosphere, in addition to other factors such as magnetic field strength and frequencies. In fact, more extended halos are seen around the chromospheric active regions (Brown et al. 1992; Braun et al. 1992b). A complete theory of acoustic wave scattering by an inclined field should give a better quantitative understanding of how scattering influences the suppression/enhancement as a function of height.

We have shown qualitatively that even small-scale magnetic features show a trend in acoustic power suppression similar to large-scale magnetic structures, but a quantitative investigation would require better understanding of the formation heights of the spectral lines. The response functions of the CH molecular line and Ni (also Fe) spectral line, which are used to measure the intensity and Doppler velocity signals, respectively, are expected to be different at different heights in the solar atmosphere. It is also possible that they have relative shifts between the magnetic and non-magnetic plasmas. Thus, it is possible that there will be some systematic error in the fractional power ratios. We have investigated other data sets and our preliminary results suggest that the suppression in acoustic power at small scales, just like large-scale fields, is independent of the spectral line and instrument. However, caution is needed at this stage as observations at a very high spatial resolution can always open possibilities to deal with many of the questions we are trying to address below in a much more effective way.

The similarity between the behavior of acoustic waves at the sites of large- (generated by a global dynamo mechanism) and small-scale features (considered in the present study, which could possibly originate from a local dynamo mechanism) is very interesting to note (e.g., plots like Figure 4 obtained from the results of earlier works correspond to the acoustic power in sunspots and plages). All the magnetic elements, irrespective of their size, appear to be subjected to and dominated by the surface effects and interact in a similar way with their surroundings.

Further, the fact that different lines (e.g., ground-based observations of the Fe I 557.6 nm line used by Thomas & Stanchfield 2000, the Ni I 676.8 nm line used in the present study and also for many earlier studies of active regions, and the first results obtained from *SDO*/HMI, which used the Fe I 617.3 nm line) with different magnetic sensitivities and heights of formation show ring-like regions with enhanced acoustic power in the high-ν band for both large and small magnetic structures should rule out the argument that it could be the sole property of the line that is used for this study. For example, Tripathy et al. (2007) used data from three different spectral lines (Ni I 676.8 nm from the Global Oscillation Network Group, K I 769.9 nm from the Magneto-Optical Filters at Two Heights (MOTH), and Na I 589.0 nm from MOTH and the Mount Wilson Observatory. Note that the Ni and K lines are formed in the photosphere while the Na line is formed in the lower chromosphere) at different heights in the solar atmosphere to analyze the variation of the acoustic power with height.

Thomas & Stanchfield (2000) discuss the suppression of intensity oscillations seen in Ca II K (which form in the lower to middle chromosphere). Since all Ca II K features have photospheric counterparts when observed in high-resolution *G*-band imaging, it remains to be seen if the intensity power suppression seen in the chromospheric Ca II line is a result of already suppressed *G*-band intensity oscillations in the lower atmosphere.

From this study we conclude that, irrespective of size and generation mechanism, the presence of any magnetic element (from large to small in spatial size) and its respective interaction with the trapped *p*-modes and running waves are the same. However, the strength of the interaction varies with respect to the magnetic field strength and also depends on the size of the structure. In other words, the same physical mechanisms are responsible and cause the power suppression (below 5.5 mHz) seen over strong magnetic field regions and the enhancement of "acoustic halos" (above 5.5 mHz) seen in the boundaries of magnetic elements both in magnetically active regions and the quiet Sun magnetic field. A detailed study of the CLV of the above-mentioned interactions will provide an important link toward understanding the nature and source(s) of the "acoustic halos," which has been debated for a long time.

L.P.C. thanks Craig DeForest for many useful suggestions and stimulating discussions during his visit to Southwest

Research Institute, Boulder. *Hinode* is a Japanese mission developed and launched by ISAS/JAXA, collaborating with NAOJ as a domestic partner, NASA and STFC (UK) as international partners. The scientific operation of the *Hinode* mission is conducted by the *Hinode* science team organized at ISAS/JAXA. This team mainly consists of scientists from institutes in the partner countries. Support for the post-launch operation is provided by JAXA and NAOJ (Japan), STFC (UK), NASA (USA), ESA, and NSC (Norway). Data are provided by the *SOHO*/MDI consortium. *SOHO* is a project of international cooperation between ESA and NASA. We acknowledge the courtesy of NASA/*SDO* and the AIA, EVE, and HMI science teams. The authors are grateful to P. H. Scherrer and R. S. Bogart for providing them with the tracked and mapped magnetogram data cubes.

We also thank an anonymous referee for useful suggestions that led to many improvements.

REFERENCES

Berger, T. E., & Title, A. M. 2001, ApJ, 553, 449
Bogdan, T. J., Hindman, B. W., Cally, P. S., & Charbonneau, P. 1996, ApJ, 465, 406
Braun, D. C. 1995, ApJ, 451, 859
Braun, D. C., & Duvall, T. L., Jr. 1990, Sol. Phys., 129, 83
Braun, D. C., Duvall, T. L., Jr., & Labonte, B. J. 1987, ApJ, 319, L27
Braun, D. C., Duvall, T. L., Jr., Labonte, B. J., et al. 1992a, ApJ, 391, L113
Braun, D. C., Labonte, B. J., & Duvall, T. L., Jr. 1990, ApJ, 354, 372
Braun, D. C., Lindsey, C., Fan, Y., & Jefferies, S. M. 1992b, ApJ, 392, 739
Brown, T. M., Bogdan, T. J., Lites, B. W., & Thomas, J. H. 1992, ApJ, 394, L65
de Wijn, A. G., Stenflo, J. O., Solanki, S. K., & Tsuneta, S. 2009, Space Sci. Rev., 144, 275
Freeland, S. L., & Handy, B. N. 1998, Sol. Phys., 182, 497
Gizon, L., Schunker, H., Baldner, C. S., et al. 2009, Space Sci. Rev., 144, 249
Gordovskyy, M., Jain, R., & Hindman, B. W. 2009, ApJ, 694, 1602
Hanasoge, S. M. 2009, A&A, 503, 595
Hindman, B. W., & Brown, T. M. 1998, ApJ, 504, 1029
Hindman, B. W., & Jain, R. 2008, ApJ, 677, 769
Jain, R., & Haber, D. 2002, A&A, 387, 1092
Jain, R., Hindman, B. W., Braun, D. C., & Birch, A. C. 2009, ApJ, 695, 325
Jain, R., Hindman, B. W., & Zweibel, E. G. 1996, ApJ, 464, 476
Khomenko, E., & Collados, M. 2009, A&A, 506, L5
Kitiashvili, I. N., Kosovichev, A. G., Mansour, N. N., & Wray, A. A. 2011, Sol. Phys., 268, 283
Kosugi, T., Matsuzaki, K., Sakao, T., et al. 2007, Sol. Phys., 243, 3
Leighton, R. B., Noyes, R. W., & Simon, G. W. 1962, ApJ, 135, 474
Lites, B. W., White, O. R., & Packman, D. 1982, ApJ, 253, 386
Scherrer, P. H., Bogart, R. S., Bush, R. I., et al. 1995, Sol. Phys., 162, 129
Schunker, H., & Braun, D. C. 2011, Sol. Phys., 268, 349
Spruit, H. C. 1984, in Proc. Small-Scale Dynamical Processes in Quiet Stellar Atmospheres Conf., ed. S. L. Keil (Boulder, CO: National Solar Observatory), 249
Suematsu, Y., Tsuneta, S., Ichimoto, K., et al. 2008, Sol. Phys., 249, 197
Thomas, J. H., & Stanchfield, D. C. H., II. 2000, ApJ, 537, 1086
Tripathy, S., Jain, K., Hill, F., et al. 2007, BAAS, 38, 130
Tsuneta, S., Ichimoto, K., Katsukawa, Y., et al. 2008, Sol. Phys., 249, 167
Woods, D. T., & Cram, L. E. 1981, Sol. Phys., 69, 233